CHAPTER IV

RESULTS AND DISCUSSION

4.1   Results and Discussion

4.1.1 Investigation of phase compositions

Phase compositions of as-prepared LB-LA, LB-LA (220), and LB-LA (220)-CNT are investigated by PXD, FTIR, and B 1s XPS techniques. The diffraction pattern of LB-LA shows the signals of $LiAlH_4$, $LiBH_4$, Li_3AlH_6, and Al/LiH (Figure 4.1(a)), while those of LB-LA (220) and LB-LA (220)-CNT reveal comparable phases of $LiBH_4$ and Al/LiH (Figure 4.1(b) and (c)). Due to small and broad diffraction peaks of $LiBH_4$ observed in PXD patterns, especially those of LB-LA (220) and LB-LA (220)-CNT (Figure 4.1(b) and (c)), FTIR and B 1s XPS experiments are further carried out to track B-containing phases.
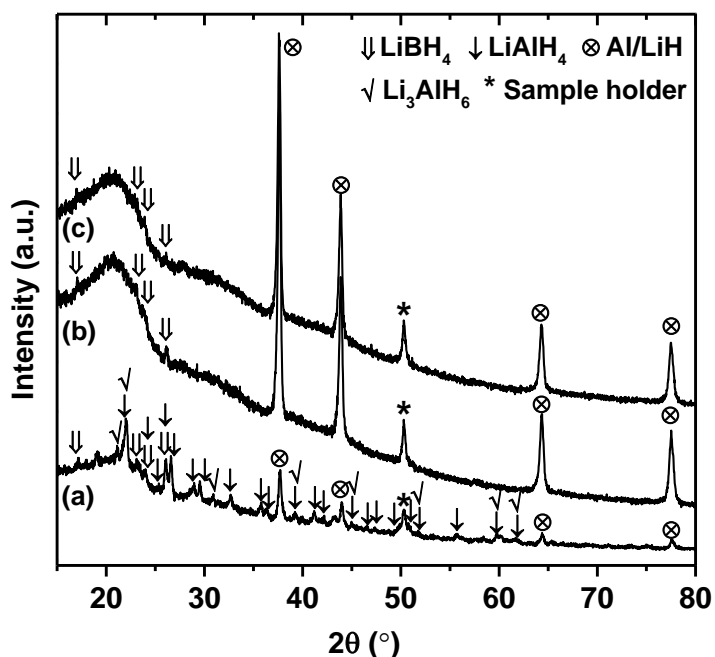

Figure 4.1 PXD spectra of as-prepared LB-LA (a), LB-LA (220) (b), and LB-LA (220)-CNT (c).

FTIR spectra of all as-prepared samples show vibrational peaks of B–H stretching and bending of $LiBH_4$ (2387-2227 and 1122 cm^{-1}, respectively) (Zhao et al., 2017), O–H bending of air and/or moisture contamination during experiments (1636 cm^{-1}) (Rapee Gosalawit-Utke et al., 2014), and B–O asymmetric stretching due to oxidation of $LiBH_4$ (1600-1300 cm^{-1}) (B€osenberg, 2010; Kamitsos, Karakassides, and Chryssikos, 1987) (Figure 4.2).
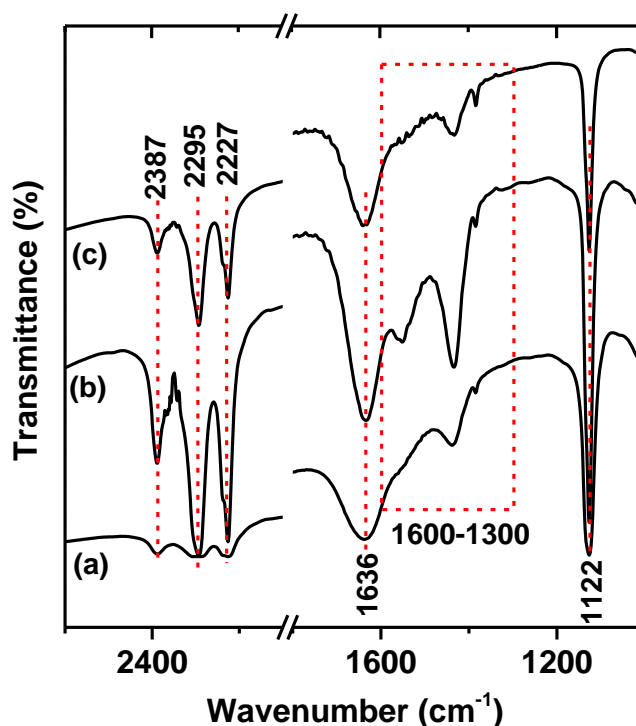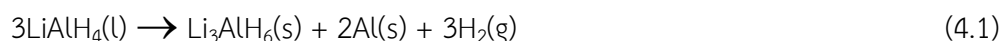

Figure 4.2 FTIR spectra of as-prepared LB-LA (a), LB-LA (220) (b), and LB-LA (220)-CNT (c).

Moreover, B 1s XPS spectra of all as-prepared samples show characteristic peaks of B–H bond of $LiBH_4$ (187.8-188.3 eV) and B–O bond of B_2O_3 due to oxidation of $LiBH_4$ (192 eV) (Figure 4.3) (Sophida Thiangviriya and Rapee Utke, 2016; U.S. Department of Commerce, 2012; Deprez et al., 2011). The signal of B–O bond implies oxidation with air and/or moisture of B-containing phases, i.e. $LiBH_4$ and/or amorphous B obtained from decomposition of $LiBH_4$ during ball milling. Thus, the weak $LiBH_4$ diffraction peaks in LB-LA (220) and LB-LA (220)-CNT (Figure 4.1(b) and (c)) can be explained by nanocrystallite size and/or amorphous state due to ball milling. The formation of Li_3AlH_6 and Al/LiH detected in LB-LA suggests partial dehydrogenation of $LiAlH_4$ (equation (4.1)) during ball milling. In the case of as-prepared LB-LA (220) and LB-LA (220)-CNT, the signal of Al/LiH hints at complete dehydrogenation of $LiAlH_4$ to LiH and Al at 220 °C (equation (4.1) and (4.2)).
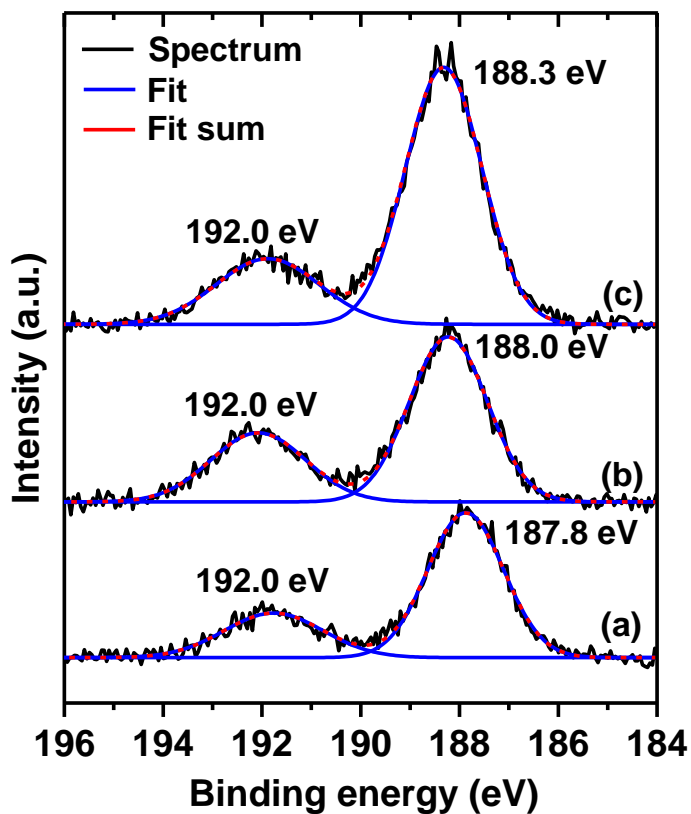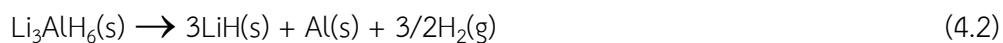
$$3LiAlH_4(l) \longrightarrow Li_3AlH_6(s) + 2Al(s) + 3H_2(g) \tag{4.1}$$

$$Li_3AlH_6(s) \longrightarrow 3LiH(s) + Al(s) + 3/2H_2(g) \tag{4.2}$$

Figure 4.3 B 1s XPS spectra of as-prepared LB-LA (a), LB-LA (220) (b), and LB-LA (220)-CNT (c).

4.1.2 Morphological studied

The morphology of all as-prepared samples is characterized by optical microscopy. The LB-LA (220) and LB-LA (220)-CNT (Figure 4.4B and C) show smaller particles and less agglomeration as compared with LB-LA (Figure 4.4A). This confirms that particle size reduction can be obtained after ball milling of dehydrogenated LB-LA quenched at 220 °C, leading to high reactive surface area and good dispersion of all phases.
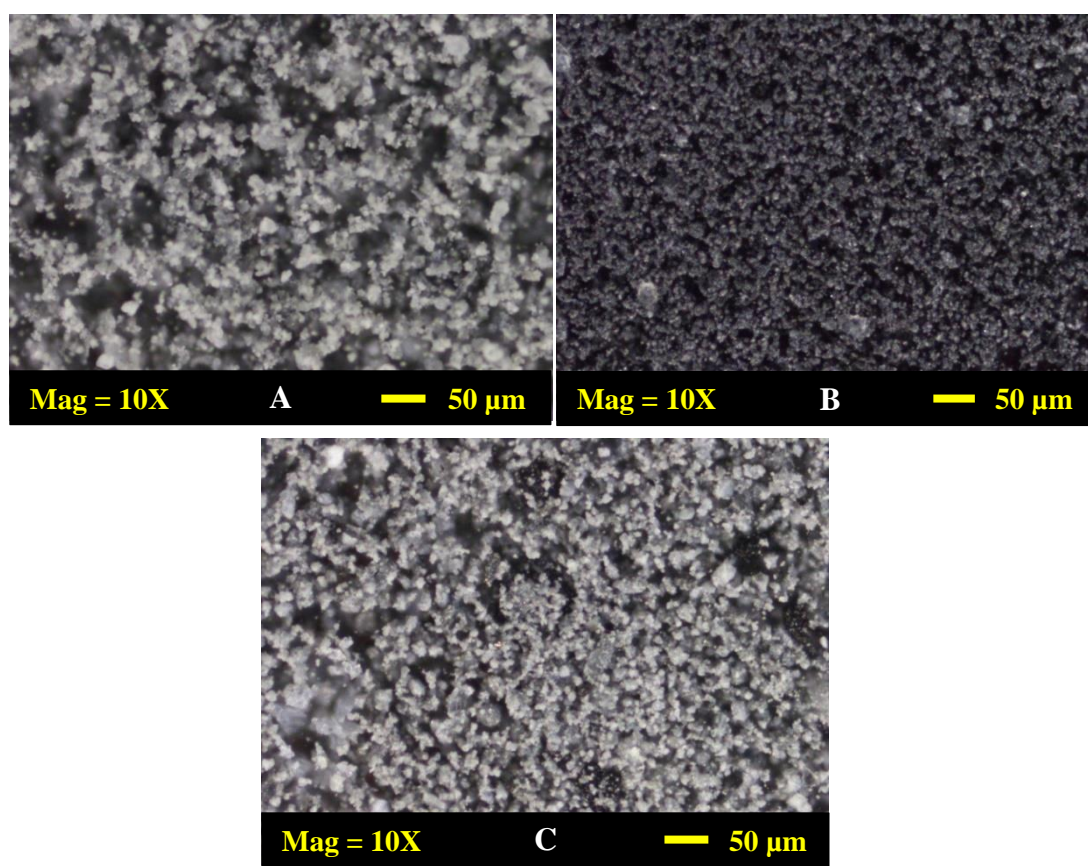
Figure 4.4 Micrographs of LB-LA (A), LB-LA (220) (B), and LB-LA (220)-CNT (C).

4.1.3 The first dehydrogenation kinetics

The 1st dehydrogenation kinetics (T= 400 °C and p(H$_2$)= 7 mbar H$_2$) of all as-prepared samples is investigated. The LB-LA releases hydrogen in two steps with total storage capacity of 6.2 wt. % H$_2$ (Figure 4.5), approaching the results from the previous studies (6.10 wt. % H$_2$) (Praphatsorn Plerdsranoy and Rapee Utke, 2015). The first-step reaction (T= 100-250 °C) rapidly liberating ~4.0 wt. % H$_2$ within 2 h agrees with decompositions of LiAlH$_4$ and Li$_3$AlH$_6$ (equations (4.1) and (4.2)). For the 2nd step corresponding to decomposition of LiBH$_4$, onset temperature at 364 °C is observed with storage capacity of 2.2 wt. % H$_2$ within 6 h. For LB-LA (220) and LB-LA (220)-CNT, single-step dehydrogenation is detected (Figure 4.5). The 1st step reaction is not observed due to complete dehydrogenation of LiAlH$_4$ during sample preparation, in accordance with PXD results (Figure 4.1(b) and (c)). During the 2nd step, decomposition of LiBH$_4$ releases 2.7-3.0 wt. % H$_2$ within 2 h (~three times faster kinetics) at significant lower onset temperature of 244 °C with respect to LB-LA (ΔT= 120 °C). Although LB-LA (220) and LB-LA (220)-CNT liberate less hydrogen than LB-LA due to

complete decomposition of LiAlH$_4$ during sample preparation, faster dehydrogenation kinetics and significant reduction of onset dehydrogenation temperature of thermally stable LiBH$_4$ can be obtained. By ball milling of LB-LA (220), particle size reduction and good distribution of all phases (Figure 4.4B) result in de/rehydrogenation kinetic improvement (Choi, Lu, Sohn, and Fang, 2011). Moreover, good particle dispersion, especially Al in LiBH$_4$ matrix favors the formation of AlB$_2$ and other active species during dehydrogenation of LiBH$_4$. These active phases lead not only to sorption kinetic improvement of LiBH$_4$ (Figure 4.5) but also reversibility of LiAlH$_4$ and/or Li$_3$AlH$_6$.
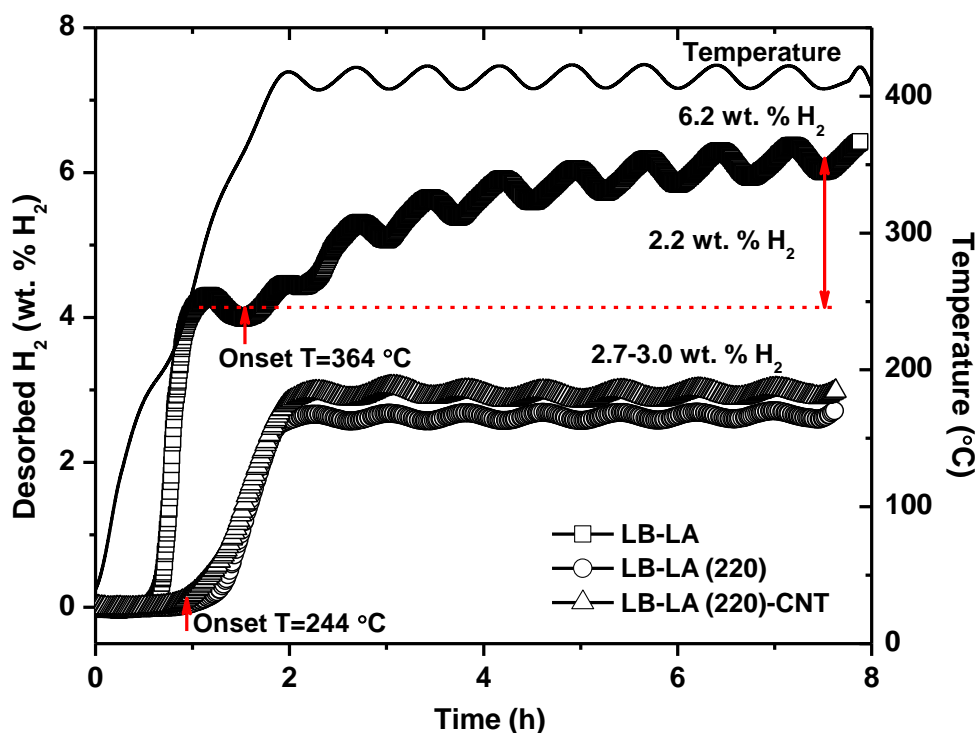

Figure 4.5 The 1st dehydrogenation kinetics of as-prepared LB-LA, LB-LA (220), and LB-LA (220)-CNT.

4.1.4 Reaction mechanisms

Reaction mechanisms during dehydrogenation of all samples are further characterized by PXD, FTIR, and solid-state ^{27}Al MAS NMR techniques. All dehydrogenated samples show comparable diffraction patterns of Al/LiH together with LiAlO$_2$ and Li$_2$O (LB-LA (220) and LB-LA (220)-CNT) due to oxidation of Li-containing phases and LiAl, respectively (Figure 4.6(b) and (c)). The FTIR spectra of all samples reveal vibrational peaks of B–H stretching and bending of LiBH$_4$ (2388-2226 and 1126 cm^{-1}, respectively), O–H bending of contamination

(1634 cm^{-1}), B–O asymmetric stretching due to oxidation of LiBH$_4$ and/ or amorphous B (1600-1300 cm^{-1}), and [B$_{12}$H$_{12}$]$^{2-}$ of Li$_2$B$_{12}$H$_{12}$ (2486 cm^{-1}) (Figure 4.7). The formation of Al/LiH, amorphous B, and Li$_2$B$_{12}$H$_{12}$ observed in dehydrogenated powder of LB-LA (Figure 4.6(a) and 4.7(a)) suggests individual decompositions of LiAlH$_4$ (equation (4.1) and (4.2)) and LiBH$_4$ (equation (4.3) and (4.4)). Moreover, the relative peak area of LiBH$_4$ vibrations (both stretching and bending at 2388-2226 and 1126 cm^{-1}, respectively) with respect to other phases in dehydrogenated LB-LA (220) and LB-LA (220)-CNT is significantly lower than that of LB-LA. This implies effective decomposition of thermally stable LiBH$_4$ in LB-LA (220) and LB-LA (220)-CNT, corresponding to superior kinetics and hydrogen content released from LB-LA (220) and LB-LA (220)-CNT compared to LB-LA (Figure 4.5).
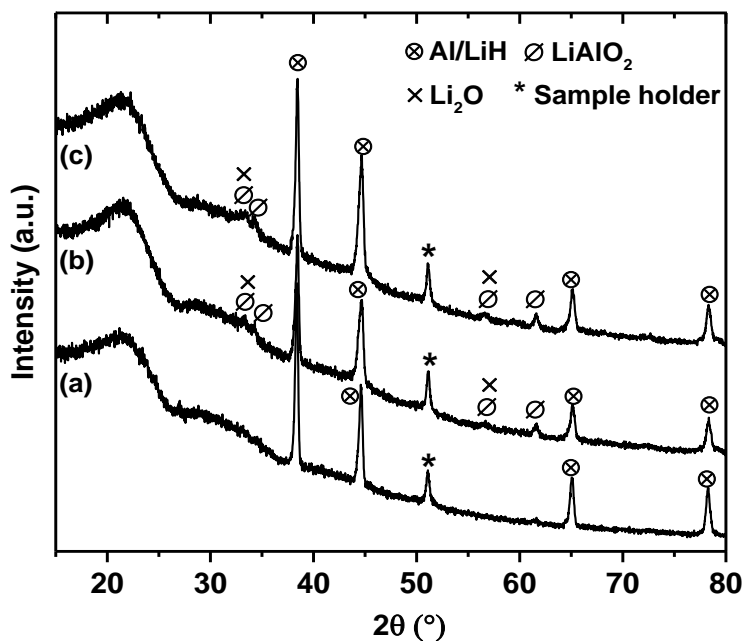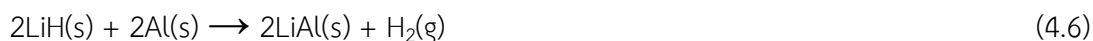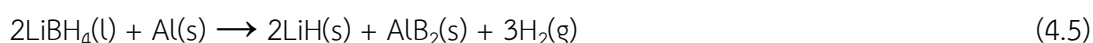
$$LiBH_4(l) \longrightarrow LiH(s) + B(s) + 3/2H_2(g) \tag{4.3}$$

$$LiBH_4(l) \longrightarrow 1/12Li_2B_{12}H_{12}(s) + 5/6LiH(s) + 13/12H_2(g) \tag{4.4}$$

$$2LiBH_4(l) + Al(s) \longrightarrow 2LiH(s) + AlB_2(s) + 3H_2(g) \tag{4.5}$$

$$2LiH(s) + 2Al(s) \longrightarrow 2LiAl(s) + H_2(g) \tag{4.6}$$
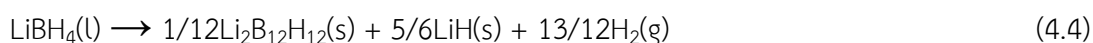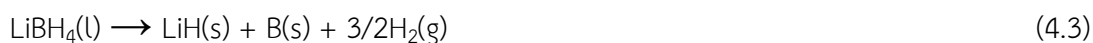

Figure 4.6 PXD spectra of dehydrogenated LB-LA (a), LB-LA (220) (b), and LB-LA (220)-CNT (c).
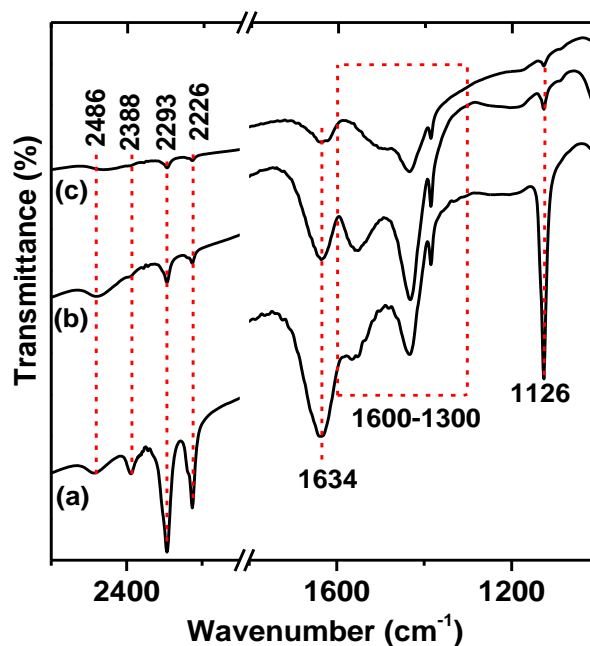
Figure 4.7 FTIR spectra of dehydrogenated LB-LA (a), LB-LA (220) (b), and LB-LA (220)-CNT (c).

In addition, Al-containing phases in dehydrogenated LB-LA (220) and LB-LA (220)-CNT are investigated by solid-state ^{27}Al MAS NMR technique. Both samples reveal characteristic peaks of metallic Al (1638 ppm) and doublet of β-LiAlO$_2$ (13 and 80 ppm) (Figure 4.8), approaching values in previous reports of 1640 ppm and doublet at 11.9 and 77.7 ppm for Al and β-LiAlO$_2$, respectively (Soru et al., 2014; Choi et al., 2011). Moreover, the resonance peaks of AlB$_2$ and β-LiAl (or γ-[Li$_3$Al$_3$]) at 865 and 393 ppm, respectively (Soru et al., 2014; Choi et al., 2011), are observed in LB-LA (220) (Figure 4.8(a)). The formation of AlB$_2$ is due to dehydrogenation of LiBH$_4$ via reacting with Al (equation (4.5)), while that of LiAl is from reaction between LiH and Al (equation (4.6)) (Choi et al., 2011).
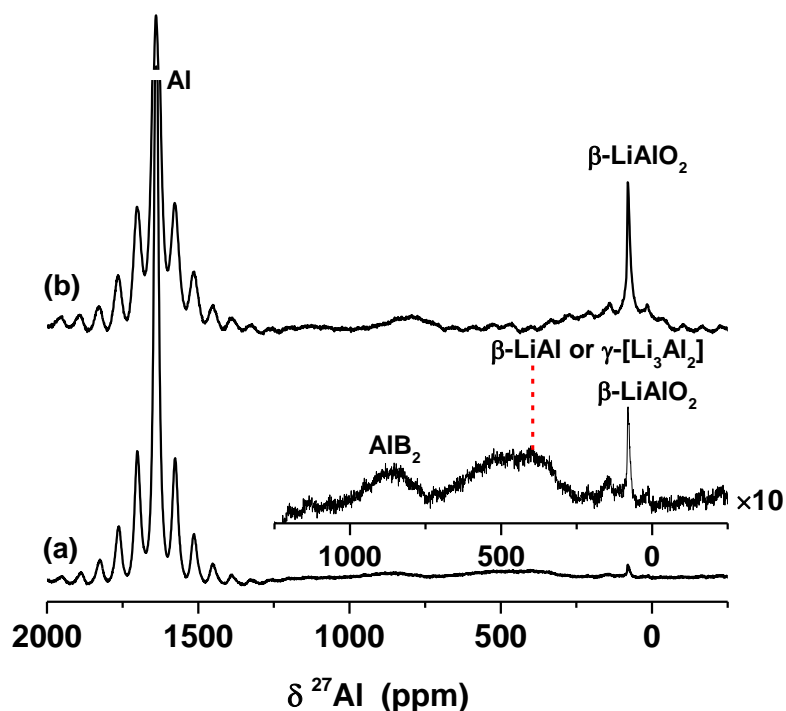
Figure 4.8 Solid-state ^{27}Al MAS NMR spectra of dehydrogenated LB-LA (220) (a) and LB-LA (220)-CNT (b).

Considering phase composition in dehydrogenated products, several step decompositions of LB-LA (220) and LB-LA (220)-CNT are summarized as follows. Both samples start with complete dehydrogenation of LiAlH$_4$ to produce LiH and Al (equation (4.1) and (4.2)) and melting of LiBH$_4$. Afterward, molten LiBH$_4$ proceeds by different mechanisms of (i) individual decomposition to LiH with either amorphous B (equation (4.3)) or Li$_2$B$_{12}$H$_{12}$ (equation (4.4)) and (ii) reaction with Al to form LiH and AlB$_2$ (equation (4.5)) (only LB-LA (220)). The LiH further reacts with Al to produce LiAl, which is possible at T >400 °C under low hydrogen pressure (equation (4.6)) (Liu et al., 2016; Meggouh, Grant and Walker, 2011; Choi et al., 2011). The formations AlB$_2$ and LiAl in dehydrogenated LB-LA (220), benefiting reversibility of LiBH$_4$ and LiAlH$_4$ (Liu et al., 2016; Hansen et al., 2013) can be achieved due to enhanced surface interaction between Al with molten LiBH$_4$ and LiH obtained from particle size reduction via ball milling. In the case of LB-LA (220)-CNT, the disappearance of AlB$_2$ might be due to the fact that dispersed MWCNTs in hydride matrices prevent contact between molten LiBH$_4$ and metallic Al.

4.1.5 Dehydrogenation kinetics and reversibility

Furthermore, dehydrogenation kinetics and reversibility of LB-LA, LB-LA (220), and LB-LA (220)-CNT (T= 400 °C and p(H$_2$)= 7 mbar) are characterized by titration measurements.

Hydrogen content produced from LB-LA during the 2nd cycle is 2.3 wt. % H_2 (Figure 4.9). For modified samples, LB-LA (220) releases comparable hydrogen content in the range of 2.5-2.8 wt. % H_2 within 3 h for three de/rehydrogenation cycles, while LB-LA (220)-CNT liberates 2.0-3.0 wt. % H_2 within 3-5 h (Figure 4.9). During the 1st cycle, LB-LA (220) and LB-LA (220)-CNT reveal comparable onset dehydrogenation temperatures of 246 °C, corresponding to decomposition of $LiBH_4$. During the 2nd and 3rd cycles, LB-LA (220) shows two-step decomposition at onset temperatures of 160 and 318 °C with storage capacities of ~0.5 and 2.0 wt. % H_2, respectively (Figure 4.9A), corresponding to dehydrogenation of $LiAlH_4$ (and/or Li_3AlH_6) and $LiBH_4$. For LB-LA and LB-LA (220)-CNT, only decomposition of $LiBH_4$ (2.0-2.3 wt. % H_2) is detected at a comparable onset temperature of 318 °C (Figure 4.9B). Thus, $LiAlH_4$ (and/or Li_3AlH_6) and $LiBH_4$ can be reproduced after rehydrogenation of LB-LA (220), whereas LB-LA and LB-LA (220)-CNT show recovery of only $LiBH_4$.
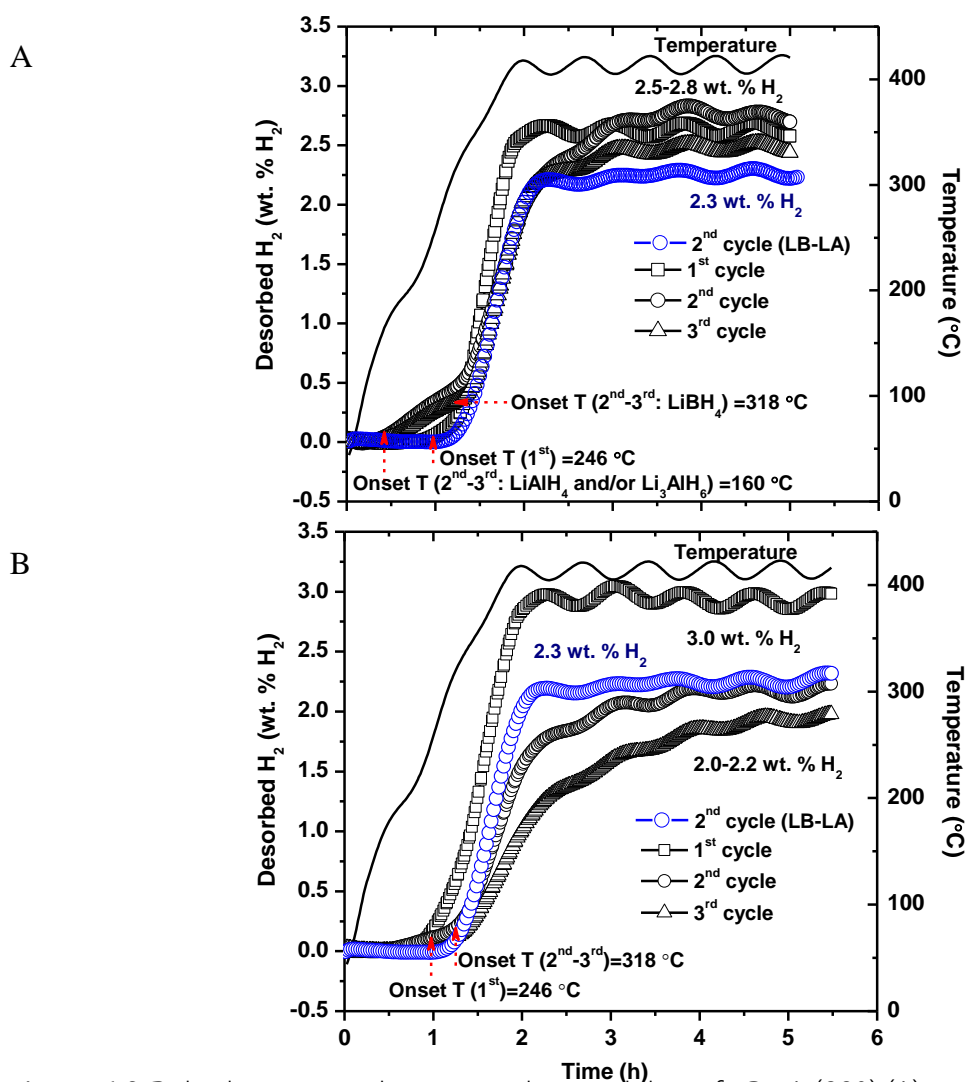

Figure 4.9 Dehydrogenation kinetics and reversibility of LB-LA (220) (A) and LB-LA (220)-CNT (B) with respect to LB-LA.

To further confirm the reversibility of hydride composite, chemical compositions in rehydrogenated LB-LA (220) and LB-LA (220)-CNT are characterized by PXD, FTIR, and ^{27}Al MAS NMR techniques. Comparable diffraction peaks of Al/LiH and Li_2O observed in rehydrogenated LB-LA (220) and LB-LA (220)-CNT indicate incomplete reversibility of $LiAlH_4$ and oxidation of Li-containing phases, respectively (Figure 4.10).In the case of FTIR results, rehydrogenated LB-LA (220) and LB-LA (220)-CNT reveal strong B–H vibrations of $LiBH_4$ (2388-2226 and 1128 cm^{-1} for stretching and bending, respectively) with respect to other phases (Figure 4.11), suggesting reversibility of $LiBH_4$. However, the clear vibrational peak of $Li_2B_{12}H_{12}$ at 2482 cm^{-1} hints at irreversibility of this thermally stable phase, corresponding to deficient hydrogen content released from the decomposition of $LiBH_4$ during the 2nd-3rd cycles (onset at 318 ºC) (Figure 4.9).
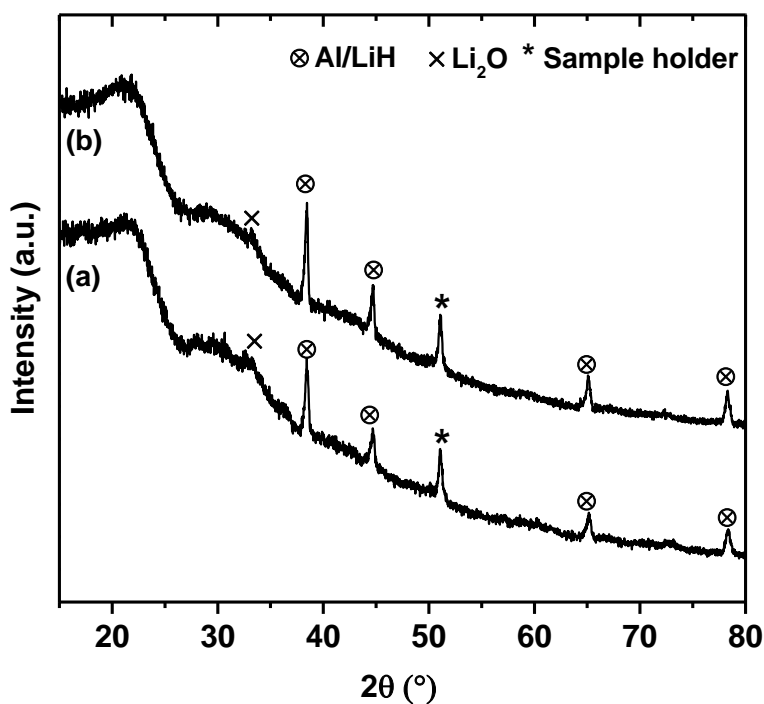

Figure 4.10 PXD spectra of rehydrogenated LB-LA (220) (a) and LB-LA (220)-CNT (b).
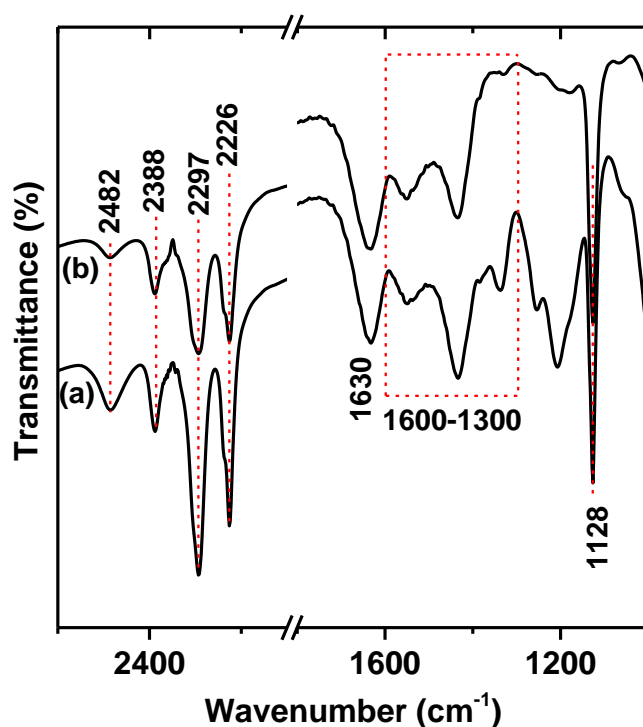
Figure 4.11 FTIR spectra of rehydrogenated LB-LA (220) (a) and LB-LA (220)-CNT (b).

For ^{27}Al MAS NMR spectra (Figure 4.12), rehydrogenated LB-LA (220) and LB-LA (220)-CNT show comparable characteristic peaks of metallic Al at 1640 ppm as well as α- and β-LiAlO$_2$ at 16.2 and 83.4 ppm, respectively (Choi et al., 2011). Moreover, the ^{27}Al MAS NMR spectrum of rehydrogenated LB-LA (220) exhibits the signals of LiAlH$_4$ and Li$_3$AlH$_6$ at 108.3 and -31.2 ppm, respectively (Figure 4.12(a)), while that of rehydrogenated LB-LA (220)-CNT reveals the chemical shift of six-coordinated oxidized Al^{III} derivatives (Al$_o$) at 65 ppm from the reaction of highly reactive Al and oxygen impurities (Figure 4.12(b)) (Wiench, Balema, Pecharsky, and Pruski, 2004). The reversibility of LiAlH$_4$ and Li$_3$AlH$_6$ after rehydrogenation of LB-LA (220) is consistent with the dehydrogenation at low onset temperature (160 °C) detected in the 2nd cycle (Figure 4.9A). Considering dehydrogenation kinetics and reversibility of LB-LA (220) and LB-LA (220)-CNT (Figure 4.9), reversibility of LiBH$_4$ in the 2nd and 3rd cycles is comparable (hydrogen content released of ~2.0-2.3 wt. % H$_2$ for both samples). Although the formation of AlB$_2$, favoring reversibility of LiBH$_4$ via reverse reaction of equation (4.6), cannot be achieved after dehydrogenation of LB-LA (220)-CNT, catalytic effects as well as enhanced hydrogen diffusion and thermal conductivity of carbon materials (MWCNTs in this study) (Ruffieux, Gr€oning, O., Bielmann, and Gr€oning, P., 2004; Adelhelm, and Jongh, 2011; Praphatsorn Plerdsranoy, Songwuit Chanthee, and Rapee Utke, 2017) benefit the reproducibility of LiBH$_4$. For LB-LA (220), the simple approach of reducing

particle size of Al obtained after decomposition of LiAlH$_4$ via ball milling encourages the formation of AlB$_2$ and LiAl. The latter leads to effective reversibility of LiBH$_4$, LiAlH$_4$, and Li$_3$AlH$_6$, and enhances hydrogen content desorbed upon cycling. Nevertheless, irreversible phases of metallic Al and Li$_2$B$_{12}$H$_{12}$ lead to lower hydrogen contents released and reproduced by both LB-LA (220) and LB-LA (220)-CNT.
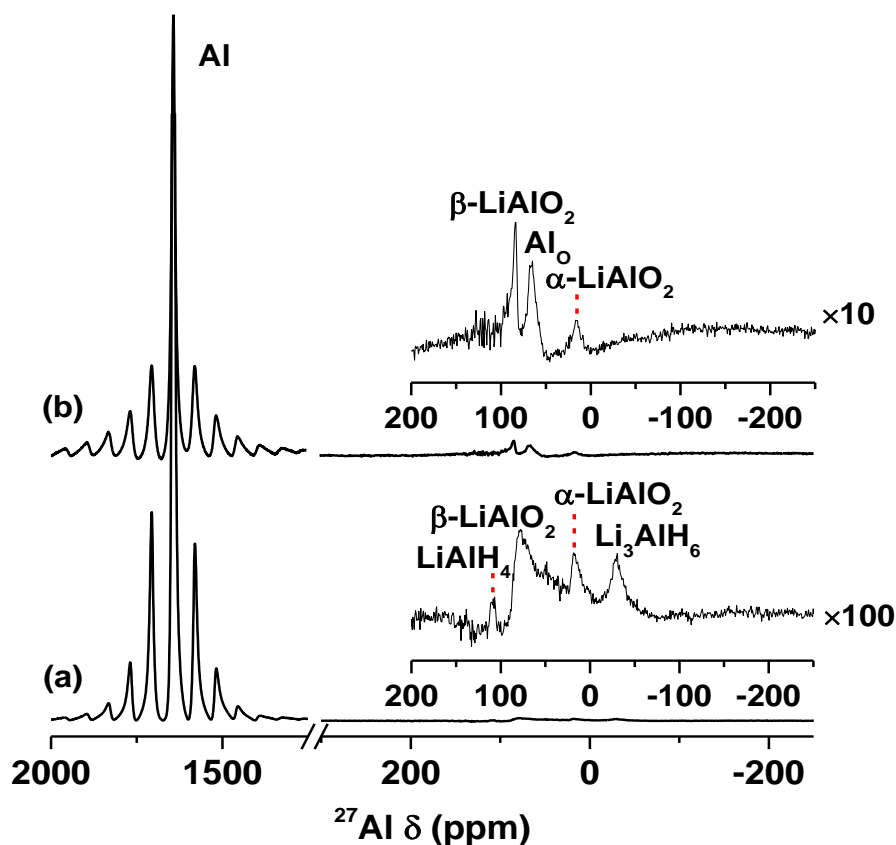

Figure 4.12 Solid-state 27Al MAS NMR spectra of rehydrogenated LB-LA (220) (a) and LB-LA (220)-CNT (b).

4.2   References

Adelhelm, P., and de Jongh, P. E. (2011). The impact of carbon materials on the hydrogen storage properties of light metal hydrides. *J. Mater Chem., 21,* 2417-2427.

B€osenberg, U., Ravnsbæk, D. B., Hagemann, H., D'Anna, V., Bonatto Minella, C., Pistidda, C., and Dornheim, M. (2010). Pressure and temperature influence on the desorption pathway of the $LiBH_4$-MgH_2 composite system. *J. Phys. Chem. C., 114*, 15212–15217.

Choi, Y. J., Lu, J., Sohn, H. Y., and Fang, Z. Z. (2011). Reaction mechanisms in the Li_3AlH_6/$LiBH_4$ and Al/$LiBH_4$ systems for reversible hydrogen storage. Part 1: H capacity and role of Al. *J. Phys. Chem. C., 115,* 6040–6047.

Choi, Y. J., Lu, L., Sohn, H. Y., Fang, Z. Z., Kim, C., Bowman Jr. R. C., and Hwang, S. J. (2011). Reaction mechanisms in the Li_3AlH_6/$LiBH_4$ and Al/$LiBH_4$ systems for reversible hydrogen storage. Part 2: solid-state NMR studied. *J. Phys. Chem. C., 115,* 6048–6056.

Deprez, E., Munoz-Maaquez, M. A., Jimenez de Haro, M. C., Palomares, F. J., Sorai, F., Dornheim, M., and Fernaandez, A. (2011). Combined X-ray photoelectron spectroscopy and scanning electron microscopy studies of the $LiBH_4$-MgH_2 reactive hydride composite with and without a Ti-based additive. *J. Appl. Phys., 109,* 014913.

Gosalawit-Utke, R., Meethom, S., Pistidda, C., Milanese, C., Laipple, D., Saisopa, T., and Dornheim, M. (2014). Destabilization of $LiBH_4$ by nanoconfinement in PMMA-co-BM polymer matrix for reversible hydrogen storage. *Int. J. Hydrogen Energy., 39,* 5019–5029.

Hansen, B. R. S., Ravnsbæk, D. B., Reed, D., Book, D., Gundlach, C., Skibsted, J., and Jensen, T. R. (2013). Hydrogen storage capacity loss in a $LiBH_4$-Al composite. *J. Phys. Chem. C., 117,* 7423–7432.

Kamitsos, E. I., Karakassides, M. A., and Chryssikos, G. D. (1987). Vibrational spectra of magnesium-sodium-borate glasses. 2. Raman and mid-infrared investigation of the network structure. *J. Phys. Chem., 91,* 1073–1079.

Liu, H., Wang, X., Zhou, H., Gao, S., Ge, H., Li, S., and Yan, M. (2016). Improved hydrogen desorption properties of $LiBH_4$ by AlH_3 addition. *Int. J. Hydrogen Energy., 41,* 22118–22127.

Meggouh, M., Grant, D. M., and Walker, G. S. (2011). Optimizing the destabilization of $LiBH_4$ for hydrogen storage and the effect of different Al sources. *J. Phys. Chem. C., 115,* 22054–22061.

Plerdsranoy, P., and Utke, R. (2015). Confined $LiBH_4$-$LiAlH_4$ in nanopores of activated carbon nanofibers. *Int. J. Hydrogen Energy., 40,* 7083–7092.

Plerdsranoy, P. Chanthee, S., and Utke., R. (2017). Compaction of $LiBH_4$-MgH_2 doped with MWCNTs-TiO_2 for reversible hydrogen storage. *Int. J. Hydrogen Energy., 42,* 978–986.

Ruffieux, P., Gr€oning, O., Bielmann, M., and Gr€oning, P. (2004). Hydrogen chemisorption on sp^2- bonded carbon: influence of the local curvature and local electronic effects. *Appl. Phys. A., 78,* 975–980.

Soru, S., Taras, A., Pistidda, C., Milanese, C., Bonatto Minella, C., Masolo, E., and Garroni, S. (2014). Structural evolution upon decomposition of the $LiAlH_4$-$LiBH_4$ system. *J. Alloy. Comp., 615,* S693–S697.

Thiangviriya, S., and Utke, R. (2016). Improvement of dehydrogenation kinetics of $2LiBH_4$-MgH_2 composite by doping with activated carbon nanofibers. *Int. J. Hydrogen Energy., 41,* 2797–2806.

U.S. Department of Commerce. (2012). *National Institute of Standards and Technology (NIST): NIST Inorganic Crystal Structure Database (ICSD) SRD 3.* Retrieved from https://srdata.nist.gov/xps/main_search_menu.aspx

Wiench, J. W., Balema, V. P., Pecharsky, V. K., and Pruski, M. (2017). Solid-state ^{27}Al NMR investigation of thermal decomposition of $LiAlH_4$. *J. Solid State Chem., 177,* 648–653.

Zhao, Y., Liu, H., Liu, Y., Wang, Y., Yuan, H., and Jiao, L. (2017). Synergistic effects of destabilization, catalysis and nanoconfinement on dehydrogenation of $LiBH_4$. *Int. J. Hydrogen Energy., 42,* 1354–1360.